



International Journal of Research in Academic World

Received: 09/October/2025

IJRAW: 2025; 4(11):203-208

Accepted: 20/November/2025

Thermogravimetric, Photoluminescence and Atomic Force Microscopy Characterization of Metal-Loaded Polyaniline and Metal Sulfide Nanostructures

¹Nidhi V Nalkande, ²RP Pawar and ^{*3}Gopalkrushna H Murhekar^{1, 2, *3}Department of Chemistry, Organic Synthesis Division, Government Vidarbha Institute of Science and Humanities, Amravati, Maharashtra, India.

Abstract

In this work, the thermal, optical, and nanoscale surface properties of pristine polyaniline (PANI), metal-loaded PANI nanocomposites (PANI–Cd, PANI–Cu, PANI–Ni), and metal sulfide nanostructures (CdS, CuS, NiS) synthesized at different precursor concentrations are systematically investigated using Thermogravimetric Analysis (TGA), Atomic Force Microscopy (AFM), and Photoluminescence (PL) spectroscopy. TGA reveals multi-step degradation behavior in PANI and enhanced thermal stability upon metal incorporation, with PANI–Ni and NiS demonstrating the highest half-decomposition temperatures and activation energies. Metal sulfides exhibit single-step high-temperature decomposition, with NiS being the most thermally stable. AFM studies show a clear evolution from amorphous granular morphology in pristine PANI to compact, highly organized nanoscale domains in metal-loaded PANI and crystalline clusters in CdS and CuS, accompanied by increased surface roughness. PL spectra of CdS and NiS nanostructures at various concentrations display broad, asymmetric emission bands in the 1.4–2.5 eV range, dominated by defect-mediated transitions involving shallow and deep trap states (E1, E2, E3). The combined results demonstrate that metal incorporation and precursor concentration significantly tune the thermal, morphological and optical behavior of the nanostructures, making them promising for applications in optoelectronics, catalysis, sensing, energy storage, and antimicrobial systems.

Keywords: Polyaniline, CdS, NiS, CuS, Thermogravimetric Analysis, Atomic Force Microscopy, Photoluminescence, Nanocomposites, Defect states.

1. Introduction

Nanostructured materials and polymer–inorganic hybrid systems have attracted considerable attention due to their tunable optical, electrical, magnetic, and catalytic properties, which are highly sensitive to composition, morphology, and defect structure [1–4]. Conducting polymers such as polyaniline (PANI), when combined with metal ions or metal chalcogenides, form nanocomposites that exhibit synergistic behavior, including improved charge transport, enhanced redox activity, and increased environmental stability [5–7]. Metal sulfides such as CdS, CuS, and NiS, in particular, are well-known semiconductor materials with size- and defect-dependent optical and electronic properties, making them suitable for applications in photovoltaics, photocatalysis, sensing, and bioimaging [8–11]. For such hybrid and inorganic nanostructures, a comprehensive understanding of their thermal stability, surface morphology, and defect-related optical behavior is crucial to optimize their performance in real-world applications. Thermogravimetric Analysis (TGA) provides information on thermal degradation, compositional stability, and residual mass, which is especially important for polymer-based nanocomposites and metal–polymer matrices

[12–14]. Atomic Force Microscopy (AFM) is a powerful tool for probing nanoscale surface topography, grain structure, and roughness, while requiring minimal sample preparation and functioning under ambient or liquid environments [3]. Photoluminescence (PL) spectroscopy is an extremely sensitive probe of electronic transitions, band-edge states, and defect-related recombination in semiconductor and nanostructured systems [15–21]. In quantum dots and nanocrystals, PL behavior is strongly influenced by quantum confinement, surface passivation, and the presence of vacancies or interstitial defects [22–31].

In the present study, pristine PANI, metal-loaded PANI nanocomposites (PANI–Cd, PANI–Cu, PANI–Ni), and metal sulfide nanostructures (CdS, CuS, NiS) synthesized at varying precursor concentrations are characterized through TGA, AFM, and PL. The primary objectives are:

- To evaluate the thermal stability and decomposition kinetics of the nanostructures using TGA and the Horowitz–Metzger kinetic model.
- To investigate nanoscale surface morphology, grain structure and roughness using AFM.
- To analyze defect-mediated photoluminescence behavior

and identify the roles of shallow and deep defect states in CdS and NiS nanocomposites.

The combined interpretation of TGA, AFM, and PL provides a coherent picture of how metal incorporation and synthesis conditions modulate the physicochemical properties of these materials, supporting their use in energy storage, optoelectronics, catalysis, environmental treatment, and antimicrobial technologies.

2. Experimental

- i). **Materials:** Aniline monomer (AR grade), oxidizing agents, metal salts of Cd, Cu, and Ni, and precursor salts for CdS, CuS, and NiS were used as received from standard commercial sources without further purification. Distilled or deionized water was used in all preparations. Supporting electrolytes and dopant acids were of analytical grade.
- ii). **Synthesis of Polyaniline (PANI):** Pristine PANI was synthesized via chemical oxidative polymerization of aniline in acidic medium. Aniline was dissolved in a suitable acid solution under constant stirring and cooled. An oxidizing agent was added dropwise to initiate polymerization. The reaction mixture was maintained under controlled temperature and stirring until a green emeraldine salt-phase PANI precipitate formed. The product was filtered, repeatedly washed to remove oligomers and residual ions, and dried at moderate temperature to obtain PANI powder.
- iii). **Synthesis of Metal-Loaded PANI Nanocomposites:** Metal-loaded PANI nanocomposites (PANI–Cd, PANI–Cu, PANI–Ni) were obtained by incorporating metal ions into the PANI matrix either during polymerization or through post-synthetic ion exchange/complexation. In a typical route, metal salt solution was added to a dispersion of PANI under controlled pH and stirring, allowing coordination between metal ions and nitrogen sites of PANI. The resulting nanocomposites were filtered, washed to remove unbound ions, and dried. The obtained powders are referred to as PANI–Cd, PANI–Cu, and PANI–Ni.
- iv). **Synthesis of Metal Sulfide Nanostructures:** CdS, CuS, and NiS nanostructures were synthesized by a precipitation route using metal salt solutions and appropriate sulfide sources. Precursor concentrations in the range 0.2–1.0 M were employed to study the effect of concentration on particle growth and properties. The metal solution was mixed with sulfide precursor under controlled conditions (stirring, temperature, and pH), leading to nucleation and growth of metal sulfide nanoparticles. The precipitates were collected by filtration or centrifugation, washed with water/ethanol, and dried at a suitable temperature. Samples were denoted as CdS 0.2 M, CdS 0.4 M, CdS 0.8 M, CdS 1.0 M and similarly NiS 0.4–1.0 M.
- v). **Thermogravimetric Analysis (TGA):** TGA measurements were carried out using a thermogravimetric analyzer equipped with a high-precision microbalance. Approximately 5–10 mg of each sample (PANI, PANI–Cd, PANI–Cu, PANI–Ni, CdS, CuS, NiS, and concentration-varied CdS/NiS) was placed in a platinum pan. The samples were heated from room temperature to about 800 °C under a controlled atmosphere at a constant heating rate ($\phi \approx 0.333 \text{ s}^{-1}$). Mass loss as a function of

temperature was recorded and represented as TGA curves. Kinetic parameters were derived using the Horowitz–Metzger method.

- vi). **Atomic Force Microscopy (AFM):** AFM measurements were performed in tapping (intermittent contact) mode to minimize sample damage and obtain high-resolution surface images. A small amount of sample powder was dispersed or gently pressed onto a suitable substrate. AFM images were recorded in ambient conditions. Topography, grain structure, and surface roughness parameters (R_a , R_q) were extracted from the 2D and 3D images using standard AFM analysis software.
- vii). **Photoluminescence (PL) Spectroscopy:** PL spectra of CdS and NiS nanostructures at different concentrations were collected using a photoluminescence spectrometer with appropriate excitation wavelength. Emission spectra were recorded in the energy range 1.4–2.5 eV (corresponding to visible–near IR region). The spectral profiles, peak positions, and band shapes were analyzed to identify band-edge and defect-related transitions, which were correlated with the structural and synthesis parameters.

3. Results and Discussion

3.1. Thermogravimetric Analysis

i). General Features and Kinetic Approach

Thermogravimetry measures the change in mass of a sample as a function of temperature or time under a controlled atmosphere. In the present study, all nanostructures exhibit one or more weight-loss steps related to moisture removal, dopant elimination, polymer chain scission, and breakdown of sulfide phases. For selected systems, kinetic parameters such as activation energy (E_a), frequency factor (Z), entropy change (ΔS) and free energy change (ΔG) were evaluated using the Horowitz–Metzger (HM) approximation for first-order decomposition.

The HM relation is given by:

$$\log\left[\log\left(\frac{W_a}{W_r}\right)\right] = \frac{E_a \theta}{2.303 R T_s^2}$$

From the slope (a) of the plot of $\log[\log(W_a/W_r)]$ vs. θ :

$$E_a = 2.303 R a T_s^2$$

The frequency factor (Z) is obtained as:

$$Z = \frac{10^b \phi E_a}{R}$$

Change (ΔG) are given by:

$$\Delta S = 2.303 R \log\left(\frac{Z h}{k T_s}\right)$$

$$\Delta G = E_a - T_s \Delta S$$

ii). Thermal Data of PANI, Metal-Loaded PANI and Metal Sulfides

The HM-derived thermal parameters of PANI, metal-loaded PANI nanocomposites and metal sulfide samples are summarized in Table 1.

Table 1: Thermal data of synthesized NPs.

NPs	Half Decomposition Temp (°C)	Activation Energy (kJ mol ⁻¹)	Frequency Factor Z (s ⁻¹)	Entropy Change $-\Delta S$ (J mol ⁻¹ K ⁻¹)	Free Energy ΔG (kJ mol ⁻¹)	Mass Loss (%)
PANI	252	72	14.46	896	456.79	69.90
PANI–Cd	246	81	16.56	987	540.92	59.90
PANI–Cu	278	87	16.56	906	549.77	52.99
PANI–Ni	262	79	14.66	976	562.48	65.77
CdS	262	84	26.46	830	500.12	55.64
CuS	289	77	16.74	898	460.39	69.97
NiS	253	73	14.43	897	456.70	69.98
CdS 1.0 M	248	80	16.57	988	540.90	59.98
CdS 0.8 M	279	89	16.59	909	549.78	52.90
CdS 0.4 M	263	78	14.69	978	562.44	65.70
CdS 0.2 M	252	72	14.46	896	456.79	69.90
NiS 1.0 M	246	81	16.56	987	540.92	59.90
NiS 0.8 M	278	87	16.56	906	549.77	52.99
NiS 0.6 M	262	79	14.66	976	562.48	65.77
NiS 0.4 M	246	81	16.56	987	540.92	59.90

iii). Discussion of Thermal Behavior

The TGA curve of pristine PANI shows three distinct weight-loss stages:

- **25–150 °C:** Initial loss of physically adsorbed water and volatile species.
- **150–350 °C:** Partial deprotonation, dopant loss and structural rearrangement of PANI chains.
- **350–650 °C:** Major decomposition of the polyaniline backbone and formation of a carbonaceous residue. Upon incorporation of metal ions, PANI–Cd, PANI–Cu, and PANI–Ni exhibit higher decomposition temperatures and increased activation energies, indicating improved thermal resistance. The delayed final decomposition suggests stronger metal–polymer coordination through nitrogen sites and enhanced cross-linking. Among the composites, PANI–Ni displays the highest ΔG and improved stability, followed by PANI–Cu and PANI–Cd, revealing the strongest binding and more rigid framework in Ni-based systems. For CdS, CuS, and NiS nanoparticles, TGA reveals a dominant high-temperature weight loss between ~550–700 °C, corresponding to breakdown of sulfide phases and conversion to metal oxides. NiS displays the highest decomposition temperature, indicating the most robust crystalline structure, whereas CdS and CuS show similar but slightly lower stability.

Variation of precursor concentration (0.2–1.0 M) in CdS and NiS further modulates thermal behavior. Higher concentration samples (0.8–1.0 M) show right-shifted degradation temperatures and lower relative mass loss, which can be attributed to better crystallinity, grain densification, and reduced surface defect density. Lower concentration samples decompose earlier due to smaller crystallite size, higher surface energy and increased defect states.

- Metal incorporation enhances thermal stability of both PANI-based composites and metal sulfides.
- PANI–Ni and NiS are the most thermally stable representatives in the respective series.
- Precursor concentration provides an effective route to tune thermal endurance and structural integrity.

These thermal characteristics validate the suitability of the

prepared materials for applications involving elevated temperatures, such as catalysis, sensing and antimicrobial deployment.

3.2. Atomic Force Microscopy (AFM)

i). Morphology of PANI and Metal-Loaded PANI

AFM images of pristine PANI show an irregular, soft granular morphology with loosely aggregated clusters, characteristic of emeraldine salt-phase PANI formed via oxidative polymerization. The surface is relatively smooth with moderate height variation, indicating largely amorphous topology.

Upon metal deposition:

- PANI–Cd exhibits broader grain distribution and increased height variation, suggesting heterogeneous nucleation sites induced by Cd coordination.
- PANI–Cu shows finer and more uniformly distributed grains than PANI–Cd, implying stronger and more homogeneous metal–polymer interaction.
- PANI–Ni displays highly condensed nano-clusters with noticeable height modulation, forming a compact and densely packed morphology.

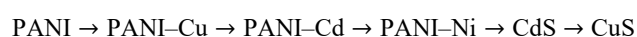
These observations confirm that metal ions act as nucleation centers and promote organized growth of PANI chains. The resulting nanocomposites exhibit grain refinement, improved surface organization, and enhanced structural rigidity, particularly in Ni-based systems.

ii). Comparison with Metal Sulfides

AFM images of CdS and CuS show surfaces that are significantly more crystalline and coarser than PANI-based samples:

- CdS forms moderately sized crystalline clusters with rough grain boundaries, indicating partial coalescence.
- CuS shows the highest surface height variation and sharp boundaries, consistent with well-developed hexagonal or layered sulfide structures.

The qualitative trend in surface height/roughness is:



This progression reflects a transition from relatively smooth, amorphous polymeric surfaces to rough, crystalline metal sulfide architectures.

Table 2: Summary of AFM interpretation

Sample	Texture	Grain Structure	Roughness Level	Structural Type
PANI	Smooth	Amorphous clusters	Low	Polymer
PANI–Cd	Moderately rough	Larger irregular grains	Medium	Composite
PANI–Cu	Uniform granular	Fine dispersed grains	Medium–High	Composite
PANI–Ni	Highly compact	Dense nano-clusters	High	Composite
CdS	Coarse particulate	Crystalline clusters	High	Nanoparticle
CuS	Sharp boundary grains	Dense crystalline texture	Highest	Nanoparticle

iii). Particle Dimensions from AFM Height Profiles

Although lateral dimensions measured by AFM are influenced by tip convolution, height (z-axis) profiles provide reliable indications of particle dimensions and roughness. Approximate height ranges are summarized in Table 3.

Table 3: Approximate particle dimensions derived from AFM height scales

Sample	Height Range (nm)	Approx. Grain Size Trend	Morphology Interpretation
PANI	~ ±38	Small, less defined	Soft amorphous polymer grains
PANI–Cd	~ –40 to +640	Larger agglomerates	Metal ion interaction increases cluster height and local aggregation
PANI–Cu	~ –41 to +34	Moderate increase	Uniform and moderately sized grains
PANI–Ni	~ –207 to +207	Dense and compact grains	Strongest ion–polymer coordination; controlled crystalline growth
CdS	~ –110 to +120	Crystalline nanoparticle clusters	Growth typical of semiconductor nanostructures
CuS	~ –291 to +337	Largest nanoscale crystalline clusters	Highly developed sulfide crystallites

Pristine PANI exhibits the smallest vertical grain dimensions and amorphous character. Metal-loaded PANI shows larger, more organized nano-domains due to nucleation effects and polymer chain reorganization. PANI–Ni presents the most controlled, dense cluster formation, while CdS and CuS reveal

highly crystalline features with significant height variation. These morphological attributes are expected to enhance electron transport, adsorption behavior, catalytic activity and antimicrobial performance, especially in Ni- and Cu-based systems.

3.3. Photoluminescence (PL) Study**i). PL Characteristics of CdS and NiS Nanocomposites**

PL spectra of CdS and NiS nanostructures synthesized at different concentrations exhibit broad, asymmetric emission bands in the energy range 1.4–2.5 eV, evidencing multiple radiative recombination pathways involving band-edge states and a distribution of defect levels. Each sample shows a characteristic emission maximum, with noticeable red or blue shifts among samples. These spectral shifts reflect changes in: Crystallite size (quantum confinement), Defect concentration and type, Dopant incorporation and surface passivation Lattice strain and non-stoichiometry. The asymmetry and low-energy tailing suggest significant contributions from deep-level transitions associated with sulfur vacancies, metal vacancies, and interstitial or antisite defects [29–31].

ii). Assignment of E1, E2 and E3 Transitions

The emission bands are categorized into three major components:

- **E1 (Green Emission):**
 - ~2.25–2.35 eV (~525–550 nm)
 - Near band-edge or shallow donor–acceptor transitions (CB → shallow levels)
 - Indicates relatively good crystallinity and low structural disorder.
- **E2 (Yellow Emission):**
 - ~1.85–2.15 eV (~580–670 nm)
 - Trap-assisted recombination via intermediate defect states (Is) within the bandgap
 - Associated with interstitials or antisite defects and partial defect passivation.
- **E3 (Red/deep-level Emission):**
 - ~1.65–1.75 eV (~710–750 nm)
 - Deep-level recombination involving vacancy states (Vs) or mid-gap traps (Vm)
 - Dominant when lattice imperfections and non-stoichiometric defects are abundant.

The schematic energy level diagram (not shown) illustrates electrons excited to the conduction band relaxing via multiple shallow and deep traps before recombining with valence-band holes, giving rise to multi-color luminescence.

Table 4: Summary of PL peak positions and corresponding electronic transitions

Sample Code	Peak Position (eV)	Approx. Wavelength (nm)	Assigned Transition	Origin/Mechanism	Interpretation
S1	~1.65–1.75	~710–750	E3 (Deep level)	Vacancy-mediated (Vs → Vm/VB)	Strong structural defects, sulfur/metal vacancies
S2	~1.85–1.95	~635–670	E2 (Mid-gap defect)	Trap-assisted recombination via intermediate defect states (Is)	Partial defect passivation with residual non-stoichiometry
S3	~2.05–2.15	~580–605	Mixed E2 + E1	Overlap of excitonic and defect-mediated transitions	Improved crystallinity and reduced deep-level contribution
S4	~2.25–2.35	~525–550	E1 (Shallow transition)	Near band-edge transitions (CB → shallow donor/acceptor states)	Better ordered lattice and fewer intrinsic defects
S5	~2.40–2.50	~495–515	Band-edge/excitonic	Direct CB–VB or excitonic recombination	Strong confinement, lower defect density and higher structural purity

iii). Defect-Mediated Optical Behavior

The PL analysis indicates that:

- Emission in the high-energy region (E1, band-edge) increases when crystallinity improves and deep defects are reduced.
- Red-shifted, broadened emission and strong E3 contributions signal higher defect density and enhanced defect-mediated recombination.
- Variations in precursor concentration and synthesis conditions modulate the balance between band-edge and defect-related emissions, enabling tuning of luminescence color and intensity.

Systems where high-energy emission dominates are more suitable for optoelectronic and light-emitting applications, while materials with strong deep-level emission may be useful for sensing, photocatalysis, and defect-based photophysics.

4. Conclusion

PANI, metal-loaded PANI nanocomposites (PANI–Cd, PANI–Cu, PANI–Ni), and metal sulfide nanostructures (CdS, CuS, NiS) synthesized at different precursor concentrations were systematically characterized by TGA, AFM, and PL techniques. Key findings can be summarized as follows: Pristine PANI exhibits characteristic multi-step degradation associated with moisture loss, dopant removal, and backbone decomposition. Metal incorporation into PANI significantly enhances thermal stability, with PANI–Ni showing the highest half-decomposition temperature and free energy of decomposition. Metal sulfides display single-step high-temperature decomposition (550–700 °C), with NiS being the most thermally stable. Higher precursor concentrations (0.8–1.0 M) improve crystallinity and delay decomposition, demonstrating synthesis-dependent thermal tuning.

PANI shows amorphous, smooth granular texture, whereas metal-loaded PANI nanocomposites display grain refinement and increased surface organization. PANI–Ni exhibits dense, compact nano-clusters indicating strong metal–polymer coordination. CdS and CuS exhibit coarse, crystalline textures with high surface roughness, CuS being the roughest and most crystalline. The roughness trend PANI → PANI–Cu → PANI–Cd → PANI–Ni → CdS → CuS reflects a transition from amorphous polymer to crystalline metal sulfide behaviour's and NiS nanostructures show broad PL emission in the 1.4–2.5 eV range dominated by defect-mediated transitions. Emission bands can be ascribed to shallow (E1), intermediate (E2) and deep (E3) defect levels, alongside band-edge excitonic transitions. The relative intensities and positions of these bands depend on particle size, defect concentration and synthesis conditions, enabling tunable luminescence. Overall, the study demonstrates that metal incorporation and precursor concentration provide effective control over thermal stability, nanoscale morphology, and defect-related optical properties of PANI-based nanocomposites and metal sulfide nanostructures. These tunable properties make the materials promising candidates for applications in optoelectronics, sensing, photocatalysis, energy storage, and antimicrobial technologies.

Acknowledgement

Author would like to express our sincere gratitude to the Department of Chemistry, G.V.I.S.H., and Amravati for providing research and library facilities.

References

1. Farber E. A history of metals. *Science*. 1960; 132:887–888

2. An L, Yu Y, Li X, Liu W, Yang H, Wu D, Yang S. Dextran-coated superparamagnetic amorphous Fe–Co nanoalloy for magnetic resonance imaging applications. *Mater Res Bull*. 2014; 49:285–290
3. Farle M. Imaging techniques: nanoparticle atoms pinpointed. *Nature*. 2017; 542:35–36
4. Ferrando R, Jellinek J, Johnston RL. Nanoalloys: from theory to applications of alloy clusters and nanoparticles. *Chem Rev*. 2008; 108:845–910
5. Qin Z, Zhang F. Surface decorated Cd_xZn_{1–x}S cluster with CdS quantum dot as sensitizer for highly photocatalytic efficiency. *Appl Surf Sci*. 2013; 285P:912–917
6. Ayelea DW, Suc W, Chou H, Pan C, Hwang B. Composition-controlled optical properties of colloidal CdSe quantum dots. *Appl Surf Sci*. 2014; 322:177–184
7. Shen S, Wang Q. Rational tuning the optical properties of metal sulfide nanocrystals and their applications. *Chem Mater*. 2013; 25:1166–1178
8. Zhou J, Yang Y, Zhang C-Y. Toward biocompatible semiconductor quantum dots: from biosynthesis and bioconjugation to biomedical application. *Chem Rev*. 2015; 115:11669–11717
9. Xu Q, Zhang Y, Tang B, Zhang C-Y. Multicolor quantum dot-based chemical nose for rapid and array-free differentiation of multiple proteins. *Anal Chem*. 2016; 88:2051–2058
10. Wang L-J, Ma F, Tang B, Zhang C-Y. Base-excision-repair-induced construction of a single quantum-dot-based sensor for sensitive detection of DNA glycosylase activity. *Anal Chem*. 2016; 88:7523–7529
11. Ma F, Li Y, Tang B, Zhang C-Y. Fluorescent biosensors based on single-molecule counting. *Acc Chem Res*. 2016; 49:1722–1730.
12. Zhou L, Gao C, Xu W. Simultaneous photoluminescence import and mechanical enhancement of polymer films using silica-hybridized quantum dots. *J Mater Chem*. 2010; 20:5675–5681
13. Zhou L, Gao C, Hu X, Xu W. One-pot large-scale synthesis of robust ultrafine silica-hybridized CdTe quantum dots. *ACS Appl Mater Interfaces*. 2010; 2:1211–1219
14. Zhou L, Gao C, Xu W, Wang X, Xu Y. Enhanced biocompatibility and biostability of CdTe quantum dots by facile surface-initiated dendritic polymerization. *Biomacromolecules*. 2009; 10:1865–1874
15. Archana J, Navaneethan M, Hayakawa Y, Ponnusamy S, Muthamizhchelvan C. Effects of multiple organic ligands on size uniformity and optical properties of ZnSe quantum dots. *Mater Res Bull*. 2012; 47:1892–1897
16. Yu D, Du K, Zhang J, Wang F, Chen L, Zhao M, Bian J, Feng Y, Jiao Y. Composition-tunable nonlinear optical properties of ternary CdSexS_{1–x} (x = 0–1) alloy quantum dots. *New J Chem*. 2014; 38:5081–5086
17. Bailey RE, Nie S. Alloyed semiconductor quantum dots: tuning the optical properties without changing the particle size. *J Am Chem Soc*. 2003; 125:7100–7106
18. Zhong X, Feng Y, Knoll W, Han M. Alloyed ZnxCd_{1–x}S nanocrystals with highly narrow luminescence spectral width. *J Am Chem Soc*. 2003; 125:13559–13563
19. Wang L, Cao L, Su G, Liu W, Xia C, Zhou H. Preparation and characterization of water-soluble ZnSe:Cu/ZnS core/shell quantum dots. *Appl Surf Sci*. 2013; 280:673–678
20. Regulacio MD, Han M-Y. Composition-tunable alloyed

- semiconductor nanocrystals. *Acc Chem Res.* 2010; 43:621–630
21. Adegoke O, Nyokong T, Forbes PBC. Structural and optical properties of alloyed quaternary CdSeTeS core and CdSeTeS/ZnS core-shell quantum dots. *J Alloys Compd.* 2015; 645:443–449
 22. Yakoubi A, Chaabane TB, Aboulaich A, Mahiou R, Balan L, Medjahdi G, Schneider R. Aqueous synthesis of Cu-doped CdZnS quantum dots with controlled and efficient photoluminescence. *J Lumin.* 2016; 175:193–202
 23. Singh S, Sabri YM, Jampaiah D, Selvakannan PR, Nafady A, Esmailzadeh Kandjani A, Bhargava SK. Easy, one-step synthesis of CdTe quantum dots via microwave irradiation for fingerprinting application. *Mater Res Bull* (in press), 2017.
 24. Zhong XH, Han MY, Dong ZL, White TJ, Knoll W. Composition-tunable $\text{Zn}_x\text{Cd}_{1-x}\text{Se}$ nanocrystals with high luminescence and stability. *J Am Chem Soc.* 2003; 125:8589–8594.
 25. Yin Y, Alivisatos AP. Colloidal nanocrystal synthesis and the organic-inorganic interface. *Nature.* 2005; 437:664–670
 26. Eaton DF. Reference materials for fluorescence measurement. *Pure Appl Chem.* 1988; 60:1107–1114
 27. Schneider CA, Rasband WS, Eliceiri KW. NIH Image to ImageJ: 25 years of image analysis. *Nat Methods.* 2012; 9:671–675
 28. Rajeshwar K, de Tacconi NR, Chenthamarakshan CR. Semiconductor-based composite materials: preparation, properties, and performance. *Chem Mater.* 2001; 13:2765–2782
 29. Tongay S, Suh J, Ataca C, Fan W, Luce A, Kang JS, Liu J, Ko C, Raghunathanan R, Zhou J, Ogletree F, Li J, Grossman JC, Wu J (2013) Defects activated photoluminescence in two-dimensional semiconductors: interplay between bound, charged, and free excitons. *Sci Rep* 3:2657
 30. Veamatahau A, Jiang B, Seifert T, Makuta S, Latham K, Kanehara M, Teranishi T, Tachibana Y. Origin of surface trap states in CdS quantum dots: relationship between size dependent photoluminescence and sulfur vacancy trap states. *Phys Chem Chem Phys.* 2015; 17:2850–2858
 31. Mansur HS. Quantum dots and nanocomposites. *Wiley Interdiscip Rev Nanomed Nanobiotechnol.* 2010; 2:113–129
 32. Qian H, Li L, Ren J. One-step and rapid synthesis of high quality alloyed quantum dots (CdSe–CdS) in aqueous phase by microwave irradiation with controllable temperature. *Mater Res Bull.* 2005; 40:1726–1736
 33. Osman MA, Othman AA, El-Said WA, Abd-Elrahim AG, Abu-sehly AA. Thermal annealing and UV irradiation effects on structure, morphology, photoluminescence and optical absorption spectra of EDTA-capped ZnS nanoparticles. *J Phys D Appl Phy.* 2016; 49:055304
 34. Chen R, Li D, Liu B, Peng Z, Gurzadyan GG, Xiong Q, Sun H. Optical and excitonic properties of crystalline ZnS nanowires: toward efficient ultraviolet emission at room temperature. *Nano Lett.* 2010; 10:4956–4961
 35. Wageh S, Ling ZS, Xu-Rong X (2003) Growth and optical properties of colloidal ZnS nanoparticles. *J Cryst Growth* 255:332–337
 36. Becker WG, Bard AJ. Photoluminescence and photoinduced oxygen adsorption of colloidal zinc sulfide dispersions. *J Phys Chem.* 1983; 87:4888–4893
 37. Denzler D, Olschewski M, Sattler K. Luminescence studies of localized gap states in colloidal ZnS nanocrystals. *J Appl Phys.* 1998; 84:2841–2845
 38. Uskokovic V. Composites comprising cholesterol and carboxymethyl cellulose. *Colloids Surf B.* 2008; 61:250–261
 39. Denton AR, Ashcroft NW. Vegard's law. *Phys Rev A.* 1991; 43:3161–3164
 40. Vegard L. Die konstitution der mischkristalle und die raumfüllung der atome. *Z Physik.* 1921; 5:17–26.